

How important is the spectral ripening effect in stratiform boundary layer clouds? Studies using simple trajectory analysis

ROBERT WOOD¹

Meteorological Research Flight, Met. Office, Farnborough, UK.

SARAH IRONS and PETER R. JONAS

Physics Department, UMIST, Manchester, UK.

SUBMITTED 12th February 2001

¹*Corresponding author address:* Dr. Robert Wood, Meteorological Research Flight, Building Y46, DERA, Farnborough, Hampshire, GU14 6TD, UK
Email: robwood@meto.gov.uk

Abstract

Any population of cloud droplets forming on polydisperse condensation nuclei is thermodynamically unstable. There is no value of the supersaturation for which the growth rate of all the droplets is zero, so that if some droplets are in equilibrium then some must have positive and some negative growth rates. Droplets with positive growth rates will continue to grow at the expense of those with negative growth rates. This effect has been termed the ripening process, and has been postulated to be a potential mechanism to explain broad droplet size distributions in stratiform clouds. In this paper we use multiple parcel trajectories, derived using a simple representation of the turbulent structure, to examine the time evolution of the droplet size distribution in a non-entraining stratiform cloud. It is shown that the magnitude of the effect is critically dependent upon the mean parcel in-cloud residence time. The simulations suggest that for a stratiform clouds of $h = 400$ m thickness, and a vertical wind standard deviation of $\sigma_w = 0.6$ m s⁻¹ (typical for stratocumulus clouds in a fairly vigorous well-mixed boundary layer), the ripening effect is negligible, in that the droplet size distribution changes little with time. However, clouds with low $\sigma_w = 0.2$ m s⁻¹ (typical of weaker stratus clouds) show a marked ripening effect over a period of several hours. Ripening is observed in the numerical model in both clean and polluted aerosol distributions, with and without the presence of giant CCN. Autoconversion rates calculated from the droplet size distributions increase markedly with time as ripening takes place. It is suggested that to accurately model droplet size distributions in stratus cloud, it is necessary to take into account the distribution of in-cloud parcel residence time.

1 Introduction

The problem of modelling droplet size distributions in stratiform boundary layer cloud has been the focus of research efforts for over fifty years. The reasons why the droplet size distribution is so crucial to our understanding of cloud processes justify the considerable expense incurred: both cloud optical properties (e.g. Stephens 1978) and warm rain formation (e.g. Beard and Ochs 1993) are strongly determined by the partitioning of liquid water content amongst droplets of different sizes.

Single adiabatic parcel model ascents have provided key insights into the processes occurring to hydrophilic aerosol as they pass from subsaturated to supersaturated air (e.g. Howell 1949). Comparison between modelled and observations size distributions (e.g. Fitzgerald 1972) suggested that droplet size distributions within warm clouds were significantly broader than those modelled using a single adiabatic ascent. Subsequent improvements to observational capability have confirmed the generality of this result (e.g. Brenguier and Chaumat 2000). The work-horse of the cloud droplet measurement community is the Forward Scattering Spectrometer Probe (FSSP, PMS Inc., Boulder, USA). This instrument has been subject to a great deal of scrutiny in an attempt to validate its accuracy in counting and sizing cloud droplets (e.g. Dye and Baumgardner 1984, Baumgardner et al. 1985, Wendisch et al. 1996, Brenguier et al. 1998). There is a general consensus that droplet size distributions measured with the FSSP are artificially broadened by a number of instrumental effects including coincidence oversizing (measurement of two or more small droplets coincident in the laser beam as one larger droplet, e.g. Baumgardner et al. 1985). However, although taking into account artificial broadening effects has shown a reduction in the breadth of the measured droplet size distributions, it is not sufficient to generate agreement between measured and modelled distributions. Thus there remains a need for improved modelling methods to explain droplet size distribution breadth in warm clouds.

Recent modelling efforts (Celik and Marwitz 1999) have shown that parcels of air that remain within a cloud for significant periods of time undergo a ripening process whereby large droplets can grow at the expense of smaller droplets. This has been termed "Ostwald ripening", following pioneering observations of crystals in 1896 by W. Ostwald. Because larger droplets grow and smaller droplets shrink the effect of this process is to broaden the spectrum at both small and large sizes. Srivastava (1991) demonstrates,

using the droplet growth equation, that the difference between the squared radii of any two activated nuclei is expected to increase with time, rather than remain constant, if the effect of droplet surface tension is included. The droplet growth equation is written

$$r \frac{dr}{dt} = G (s - s_{eq}) \quad (1)$$

where r is the droplet radius, s is the supersaturation, s_{eq} is the equilibrium supersaturation, a function of the aerosol dry radius, and G is approximately constant at a particular temperature and pressure. Hence, for two activated nuclei (radii r_1 and r_2), ignoring s_{eq} , then one can write

$$r_1 \frac{dr_1}{dt} = r_2 \frac{dr_2}{dt} \quad (2)$$

so that the difference of the squared radii does not change with time. However, if the equilibrium supersaturation is not ignored, but instead the surface tension effect is retained, then this leads to a difference in squared radii that increases as time to some power α . To explain this, consider two activated droplets with different radii. Ignoring the solute effect, the larger of these droplets has a lower equilibrium supersaturation because the surface tension scales as r^{-1} . Therefore the RHS of Eqn. 1 is larger for the larger droplet, and the difference in the square of the radius will increase with time. Following Srivastava (1991), this power α can be written as

$$\alpha \approx \text{const.} \times \frac{a_2 N}{a_1 w} \quad (3)$$

where a_1 and a_2 are the dry aerosol radii, N is the total droplet concentration, and w is the vertical ascent rate. Thus, the effect is greatest with (a) large difference between dry radii of droplets, (b) large droplet concentration, and (c) low updraught speeds. Using a single adiabatic parcel model Srivastava (1991) shows how the variance of the droplet surface area distribution increases with time in a parcel ascent with a slow updraught (0.2 m s^{-1}), but that the increase becomes less important as the parcel ascent rate is increased. Korolev (1995) also demonstrated this effect in a cyclical parcel model and suggested that the broadening of the droplet size distributions is a consequence of an oscillating supersaturation field. However the simulations of Celik and Marwitz (1999) show that, by imposing a sinusoidal in-cloud motion upon their parcel following its rise into cloud, the droplet size distributions are no broader than if the parcel remains at a constant height. This seems to suggest that the super-

saturation fluctuations have little effect *per se*, and that the effect is predominantly governed by the residence time of the parcel in the cloud and the nature of the CCN supersaturation spectrum assumed. The results of Bartlett and Jonas (1972) demonstrate that a fluctuating updraught itself has little effect upon the spread of droplet sizes in an adiabatic parcel. Celik and Marwitz (1999) also examine the effects of large CCN ($0.5 < a < 1.2 \mu\text{m}$) upon the time evolution of the droplet size distribution and show that the inclusion of increasing numbers of these large nuclei has the effect of increasing the number of very large droplets, thereby speeding up the broadening process.

The major limitation of both the Korolev (1995) and Celik and Marwitz (1999) studies in addressing the problem of spectral broadening in stratiform boundary layer clouds is that the in-cloud residence time of a parcel in real boundary layer clouds is a random variable, the probability density function (pdf) of which is a complicated function of the boundary layer dynamics and cloud geometry. In this study we attempt to use an ensemble of Lagrangian parcel trajectories subject to realistic turbulent motions within the boundary layer, to address the question of whether the ripening process is of consequence to the cloud droplet size distribution within stratus and stratocumulus clouds. Section 2 contains details of the ensemble model dynamics and microphysics; section 3 describes a set of numerical simulations to examine the hypothesis that the ripening process is important in stratus/stratocumulus clouds. Calculations of autoconversion from the model size distributions are presented in section 4. Finally, section 5 provides a discussion of the consequences of the findings.

2 Trajectory ensemble model (TEM) description

The evolution of the droplet size distribution is predicted using an ensemble of trajectories whose motion is driven by a stochastic model of realistic fluctuations in the boundary layer vertical wind field. The concept of the model and microphysical evolution is similar to that of Stevens et al. (1996) who forced a trajectory ensemble model using large eddy simulation (LES) dynamical fields. However, the trajectories in this case are all adiabatic (the effects of entrainment are not simulated) and are all initialised with the same total water mixing ratio and virtual potential temperature below cloud. There is no mixing between parcels. The simulations are intended to examine the effects of parcel in-cloud

lifetime upon the droplet size distribution simply through the Ostwald ripening effect. Additional effects of extended parcel in-cloud residence time could potentially be introduced if radiative growth of droplets at the top of the cloud were included (e.g. Austin et al. 1995a), but these are not examined here.

(a) Dynamical evolution

To simulate the time evolution of the cloud droplet size distribution an ensemble of one-dimensional parcel trajectories is derived using the transilient matrix method (Nicholls 1987; Austin et al. 1995b). The transilient matrix elements are derived using the mixing potential approach first introduced in Stull (1984), and further described in Austin et al. (1995b). Input parameters are vertical wind standard deviation σ_w and Lagrangian integral timescale τ_w . The assumption that the Eulerian and Lagrangian timescales are equal is assumed so that values of the Eulerian integral lengthscale (λ_w) as measured using horizontal traverses through cloud can be used to constrain the trajectory properties. We use a 100-level domain and a timestep of $\delta t_{trans}=240$ s for generating the trajectories (i.e. parcel speed can change once every 240 seconds). Parcels are prevented from leaving the domain top (cloud top) and bottom (ground level). The Lagrangian integral time scales are derived from the resulting trajectory time series using the method of Lenschow and Stankov (1986), and are found to compare reasonably well with the desired ones (see Appendix for more complete description of dynamical formulation). Later we show that the addition of realistic motions on timescales less than δt_{trans} makes little difference to the results in this study. Similarly, the results are not highly sensitive to changes in δt_{trans} .

(b) Thermodynamic/microphysical evolution

For each simulation the trajectories are initialised at random levels below cloud base. No trajectories are initialised in the cloud as this would present difficulties in assigning liquid water content to different condensation nuclei. The pressure at each timestep is calculated using the hydrostatic equation. The temperature T along a trajectory is calculated using

$$\frac{dT}{dt} = -\Gamma_{dry}w + \frac{L_v}{c_p} \frac{dq_c}{dt} \quad (4)$$

where q_c is the liquid water content, Γ_{dry} is the dry adiabatic lapse rate, w is the vertical wind speed,

L_v is the latent heat of vapourisation, c_p is the specific heat of air at constant pressure. The liquid water content is q_c calculated by summing over the droplet size distribution

$$q_c = \frac{4}{3}\pi\rho_w \int_r \frac{dn}{dr}(r^3 - a^3)dr \quad (5)$$

which for N discrete aerosol categories is given by

$$q_c = \frac{4}{3}\pi\rho_w \sum_{i=1}^N n_i(r_i^3 - a_i^3) \quad (6)$$

where n_i is the concentration in bin i , r is the droplet radius and a is the dry aerosol radius. The number of aerosol categories used in all the simulation is $N = 60$ with logarithmic radius spacing. The smallest aerosol dry radius is $0.01 \mu\text{m}$, with dry aerosol mass doubling every two categories, giving a maximum dry size of just over $9 \mu\text{m}$.

At each timestep along the trajectory the droplet growth rate is calculated for each aerosol size category using Eqn. 1. The equilibrium supersaturation s_{eq} is a function of both the droplet and the dry aerosol size (e.g. see Pruppacher and Klett 1997):

$$s_{eq} = \exp\left(\frac{2\sigma_{w/a}}{\rho_w R_v T r}\right) \left(1 + \frac{i\epsilon M_w \rho_s a^3}{M_s (\rho' r^3 - \rho_s a^3)}\right)^{-1} - 1 \quad (7)$$

where $\sigma_{w/a}$ is the surface tension of water, R_v is the gas constant of water vapour, T is the temperature, i is the van't Hoff factor, ϵ is the mass fraction of the soluble salt in the dry aerosol, M_w and M_s are the molecular weights of the water and salt respectively, ρ_s is salt density, and ρ' is the solution density. For the simulations in this paper we set the solution density to be that of pure water, i.e. $\rho' = \rho_w$.

The prefactor G in Eqn. 1 is given by

$$G = \left[\frac{\rho_w R_v T}{e_{sat,w} D_v^*} + \frac{L_v \rho_w}{k_a^* T} \left(\frac{L_v}{R_v T} - 1 \right) \right]^{-1} \quad (8)$$

where $e_{sat,w}$ is the saturation vapour pressure, and D_v^* and k_a^* are the vapour diffusion and thermal diffusion constants respectively. Both D_v^* and k_a^* are modified to account for kinetic effects on droplet growth rate. These corrections are described in some detail in Pruppacher and Klett (1997) and differ

little from those used by Fukuta and Walter (1970). Here, we use thermal accommodation and condensation coefficients equal to 0.70 and 0.036 respectively. The kinetic corrections only significantly affect the growth of drops smaller than around $1 \mu\text{m}$.

Thermodynamic and solution corrections to the parameters L_v , $\sigma_{w/a}$, D_v^* and k_a^* are widely accepted ones presented in Celik and Marwitz (1999). There are temperature variations applied to each parameter, a pressure correction to D_v^* and a correction to the surface tension for the effects of dissolved salt.

The hydrostatic equation, the temperature equation (4) and the droplet growth equation are solved using a timestep of $\delta t_{micro} = 0.1\text{s}$ along each Lagrangian trajectory. The supersaturation is calculated from the humidity mixing ratio q_v , temperature T and pressure p at each microphysical timestep. The total moisture is a conserved variable, there is no ice, and thus

$$\frac{dq_v}{dt} = -\frac{dq_c}{dt}. \quad (9)$$

Finally, it is assumed that all aerosol particles consist entirely of ammonium sulphate. Therefore $\epsilon = 1.0$, $i = 3$, $M_s = 0.132 \text{ kg mol}^{-1}$ and $\rho_s = 1760 \text{ kg m}^{-3}$ in Eqn. 7.

Because there is no binning during the simulation, along each trajectory (in each parcel) there is a one-to-one mapping between the hydrated droplet radius and the dry aerosol radius. This mapping is lost only when size distributions are "created" in the post-processing from the ensemble of trajectories.

(c) Derivation of averaged quantities from the trajectory ensemble model

It is important to define how averaged quantities are derived from an ensemble of parcel trajectories. During the simulations there is no binning of droplet size distributions. All binning is carried out after the runs have completed. Average quantities are calculated for particular time intervals and height intervals, using the complete set of trajectories. All simulations in this study contain $N_{traj} = 200$ trajectories. Thermodynamic, dynamic and microphysical data are output once every δt_{trans} ($=240 \text{ s}$) interval, and the total duration of most of the model runs was 400 minutes ($100 \times 240 \text{ s}$). For trajectory heights distributed uniformly through the boundary layer, an average quantity would, in the mean, be

constructed from $\overline{N}_{contrib} = N_{traj}(\delta z_{ave}/z_i)(\delta t_{ave}/\delta t_{trans})$ contributing quantities, where δz_{ave} is the height interval over which the average is to be taken, δt_{ave} is the averaging period, and z_i is the boundary layer depth. For height intervals of $\delta z_{ave} = 100$ m and averaging periods of $\delta t_{ave} = 40$ minutes (10 output steps), $N_{contrib} = 200$. The number of trajectories contributing to the average quantities can never exceed N_{traj} , but may be significantly less, because each trajectory has the potential to contribute up to $(\delta t_{ave}/\delta t_{trans})$ times to an average. Trajectories that have slow vertical ascent rates are likely to contribute more times per averaging period. That each trajectory can contribute more than once to an average should not be surprising: consider two aircraft runs through the same air space used to construct an arbitrary time-space average quantity. A parcel of air that remains at the level of the aircraft can be sampled twice in constructing the average.

The mean droplet size distribution in a particular time/height interval is binned into discrete haze/droplet size intervals. In this study there are 30 size bins, with the radii of the haze/droplet bins increasing by a factor of 10 every 10 bins. The first radius bin is defined by $10^{-1.3} < r < 10^{-1.2} \mu\text{m}$ (approx. $0.050 < r < 0.063 \mu\text{m}$). In all the simulations at least 99% of all the in-cloud haze/droplets are contained within the bins chosen here ($0.050\text{-}50.1 \mu\text{m}$).

(d) Treatment of subcloud-cloud boundary

At relative humidities below cloud hydrated haze particles are not sufficiently dilute to be grown using the growth equations presented in the previous section. Growth/evaporation can become numerically unstable because of the rapid growth rates, and the behaviour of concentrated salt solutions differs significantly from ideal solutions assumed in the derivation of the growth equation. We therefore assume that small haze particles ($r_{dry} < 1\mu\text{m}$) are in equilibrium with the parcel relative humidity when $RH < 0.99$ (lower than approximately 20 m below cloud base), and use the experimental results of Tang and Munkelwitz (1994), to calculate the humidity growth factor ($=r_{wet}/a$) as a function of RH , where a is the dry aerosol radius and r_{wet} is the equilibrium hydrated aerosol radius at RH . The shortest time taken for a parcel to travel a vertical distance of 20 m given realistic downdraught speeds is around 20 s. With $RH = 0.99$, droplets with radii less than approximately $4 \mu\text{m}$ evaporate to within 10% of their equilibrium radius within 20 s. It is therefore a reasonable assumption to treat $a < 1\mu\text{m}$ haze particles

as being in equilibrium with the parcel for $a < 1\mu\text{m}$. We allow larger haze particles to grow explicitly at all RH . It is not possible to do this with all the aerosol categories because of the numerical instabilities associated with high growth rates of small droplets. A comparison of runs where all $RH < 0.99$ is explicit ($a > 1\mu\text{m}$) with the equilibrium $RH < 0.99$ growth showed very little difference in the in-cloud droplet number and mass distributions. Just below cloud base ($0.95 < RH < 1.0$) we found slightly higher concentrations (approx. 3%) of large haze particles ($r > 5\mu\text{m}$) and slightly lower concentrations (approx. 4%) of small haze particles ($2 < r < 5\mu\text{m}$), in the explicit growth run. This can be attributed to reduced lower evaporation rates for large haze particles in parcels descending through cloud-base. It is concluded that the inclusion of explicit growth for $a > 1\mu\text{m}$ particles below $RH = 0.99$ makes little difference to the in-cloud droplet size distributions.

(e) Sensitivity tests

A number of approximations have been made in the derivation of the droplet growth equation. First, it has been assumed that the heat released by condensation of vapour onto a growing droplet is rapidly dissipated by conduction. It can be shown that this assumption of steady-state droplet-environment temperature difference is a very good one apart from when the growing droplet radius is less than a factor of three larger than the dry aerosol radius. Because we have assumed that the aerosol assume immediately their equilibrium size when the relative humidity drops below 0.99 (at which the aerosol growth factor for ammonium sulphate is approximately 3.6), we do not consider the explicit growth of drops smaller than around 3.5 times the radius of the dry aerosol, and so the effects of non steady-state temperature difference should not significantly affect the results (see e.g. Pruppacher and Klett, 1997, for a discussion on approximations to the droplet growth equation). One set of model runs was performed with a timestep $\delta t_{micro}=0.01$ s, a factor of ten less than that used in all the runs presented in this study, showed that there is very little sensitivity to the microphysical timestep used. However, when the timestep is increased to $\delta t_{micro}=1$ s, it was found that some of droplets formed on the smallest aerosol were activating even though the supersaturation was found not to exceed the critical supersaturation of the aerosol. This occurred even in low updraughts.

To examine the effects of small scale turbulence upon the microphysical evolution we carried out

two identical runs with and without turbulent vertical wind fluctuations on timescales smaller than the transient timestep δt_{trans} . We superimposed the fluctuations onto existing ($\delta t_{trans}=60$ s) trajectories using a bounded cascade model fractional interpolator (Marshak et al. 1994; Cahalan et al. 1994) which gives Kolmogorov scaling down to the timestep used for the droplet growth ($\delta t_{micro}=0.1$ s). Further details of the method used to simulate small scale turbulent fluctuations is given in the appendix.

For each of the simulations above we carried out a second trajectory ensemble simulation identical in every way apart from the addition of small scale turbulence to the trajectory set. This enables an examination of the effects of small-scale fluctuations in vertical wind upon the resulting droplet size distributions. The addition of small-scale fluctuations was found to have negligible effect upon either the number or mass distributions. The fluctuations were also found not to significantly affect the time evolution of any of the calculated microphysical parameters.

3 TEM Model runs

Model runs were set up to examine the hypothesis that Ostwald ripening effects are important for the microphysical development of stratus/stratocumulus cloud. There is little dispute that Ostwald ripening would be an important factor in the microphysical development of a parcel which rose into cloud and then remained there for some hours (as in the simulations of Celik and Marwitz 1999). It also seems clear, from the simulations of Celik and Marwitz, that vertical cycling motion within cloud is not necessary to obtain a ripening effect, and in fact does not enhance the effect at all. All that is required is that the parcel has sufficient time within the cloud. Stratus and stratocumulus clouds have a fundamentally different dynamical nature than the hypothetical clouds in the study Celik and Marwitz. Air parcels in stratus/stratocumulus are continually subject to rising and falling motion and any chosen parcel only has a finite in-cloud residence time. Once a parcel passes out of the cloud and into a subsaturated region, the effects of ripening on the size distribution of particles are rapidly lost. Therefore, it is important to consider the effects of parcels passing in and out of cloud in as realistic a manner as possible, in order to quantify ripening effects in stratus/stratocumulus. The mean in-cloud residence time ($\bar{\tau}_{in}$) is a particularly important parameter, and one would expect this to scale with the large eddy turnover time.

(a) Trajectory ensembles and in-cloud residence times

Because the in-cloud residence time τ_{in} is a particularly important determinant of the propensity for Ostwald ripening, in this section we examine the statistics of in-cloud residence times for trajectories constructed using the transilient matrix approach. We compare two ensembles of trajectories; each ensemble represents conditions in a different boundary layer dynamic regime. Details of the two sets are given in Table 1. For each set the boundary layer depth was $z_i = 800$ m, with a cloud layer extending from a height of $z_b = 400$ m to the boundary layer top. Trajectory ensemble A is representative of parcel motions in a well-mixed boundary layer with fairly vigorous large convective cells: given by $\sigma_w = 0.6$ m s^{-1} and $\tau_w = 330s$. The vertical wind power spectral ($kS(k)$) peak is found at a Lagrangian lengthscale of 500-600 m. These conditions are typical of a well-mixed stratocumulus-topped boundary layer (with a convective velocity scale $w_* \approx 0.75 - 1.0$ m s^{-1}). Observations of this type of stratiform boundary layer cloud structure are numerous (e.g. Nicholls and Leighton 1986, Flight 526). Ensemble B is also representative of conditions in a well-mixed boundary layer, but with a much weaker circulation. Dynamical parameters are $\sigma_w = 0.2$ m s^{-1} , $\tau_w = 250s$, with a power spectral peak at a lengthscale of some 100-150 m. Conditions similar to these are more representative of a weakly turbulent stratus layer, one in which shear turbulent generation of TKE is more important than convective generation. Observations of this type of structure include Brost et al. (1982a,b), 17 June 1976 flight). Both ensembles consist of $N_{traj} = 200$ trajectories. The duration of each trajectory is 400 minutes.

Figure 1 shows several parameters derived from the ensemble of trajectories. For each trajectory that is in-cloud at some output timestep we calculate the time τ_{in} since the parcel last entered cloud (the in-cloud residence time). The parameter $\bar{\tau}_{in}$ is the mean value of τ_{in} over all the trajectories at a particular timestep. This is plotted for both ensembles as a function of time in Fig. 1(a). The value of $\bar{\tau}_{in}$ rapidly reaches its equilibrium value for set A because there are very few trajectories which remain in cloud for longer than 50-60 minutes (Fig. 1(c)). However, this is not the case for ensemble B for which $\bar{\tau}_{in}$ continues to increase for around 8 hours as a result of there being a significant number of parcels which remain in cloud for several hundred minutes (Fig 1(d)). Figure 1(b) shows that the standard deviation of the in-cloud residence time is similar to the mean for both ensembles. The pdfs of in-cloud residence time at times 1, 2, 6 and 10 hours show that set A reaches an equilibrium within 1 hour (i.e.

the pdfs are the same at each time) whereas set B continues to shift to larger τ_{in} as the time progresses. The dotted curves in Fig. 1(a), which match the simulated results well, take the form:

$$\bar{\tau}_{in} = \bar{\tau}_{in,\infty} \left(1 - e^{-t/t_0}\right) \quad (10)$$

where $\bar{\tau}_{in,\infty}$ is equilibrium ($t \rightarrow \infty$) value of $\bar{\tau}_{in}$ and t_0 is a time constant, where the values for $\bar{\tau}_{in,\infty}$ and t_0 are given in Table 1. Equation 10 is an empirical result, although it might be possible to derive an expression of this form from knowledge of the turbulent structure. It is clear that there is a large increase in the in-cloud residence time as the vertical wind standard deviation is reduced. We address the effect of this upon the cloud microphysics in the following section.

Figure 2 shows the effect of varying the cloud thickness upon the values of $\bar{\tau}_{in,\infty}$ and t_0 . Both these variables increase markedly with increasing cloud thickness showing that the mean residence time at infinity of a parcel within the cloud increases by around a factor of four as the cloud thickness doubles from 300 m to 600 m. In addition, it is seen that $\bar{\tau}_{in,\infty}$ is approximately the same for a 700 m thick strong circulation cloud as it is for a 200 m thick weak circulation cloud.

(b) Description of runs performed

In this paper we examine (i) weak and strong boundary layer circulations; (ii) polluted and clean air mass types; (iii) the effects of the addition of giant cloud condensation nuclei. Constant values of cloud base height $z_b = 400$ m and cloud top height $z_i = 800$ m are used. The surface pressure and temperature are 1012 hPa and 288.5 K respectively. To investigate all combinations of (i), (ii) and (iii) above we performed eight simulations detailed in Table 2. Strong circulations were carried out using trajectory ensemble A (see previous section); weak circulations used ensemble B. Polluted air was simulated using an aerosol distribution consisting of ammonium sulphate in a lognormal distribution with mode radius of $r_{mode} = 0.04\mu\text{m}$, a geometrical standard deviation of $\sigma_{geom} = 2.2$ and a concentration of $N_a = 1000$ cm^{-3} . Clean airmasses were simulated using the same lognormal distribution but with a concentration $N_a = 200$ cm^{-3} . For the runs where giant CCN were added this was taken from the spume mode parameterization described in O’Dowd et al. (1997) and references therein, assuming a wind speed of 8 m s^{-1} . The aerosol number and mass distributions are shown in Fig. 3.

(c) General features

Figure 4(top) shows the height-time series for sections of two trajectories (taken from set B). Both trajectories show the parcel rising from cloud base to close to the cloud top. The trajectory shown by the solid line takes considerably more time to reach the upper 100 metres of the cloud than the one shown by the dashed line. The dotted line shows the height-time series for a parcel with a steady ascent rate equal to the mean ascent rate of the slow fluctuating parcel. The central panel shows the radii of droplets formed on two sizes of dry nucleus ($a = 0.05\mu\text{m}$ - thin lines; $a = 0.6\mu\text{m}$ - thick lines) as a function of height for the two trajectory sections. The critical radii of the two aerosol categories shown here are 0.48 and $20.1\mu\text{m}$ respectively. Thus, the larger of the two droplets never becomes activated at any point in the ascent. The smaller of the two droplets is activated at all heights in cloud. Nevertheless the larger unactivated droplet gains mass at the expense of the smaller activated particle. This may in some senses seem counterintuitive. However, due to the curvature and salinity effects, the shape of the equilibrium supersaturation-droplet radius curve ("Kohler curve") means that it is possible that large unactivated particles can grow at the same time as smaller activated particles are evaporating at the same supersaturation. Also shown in the central panel of Fig. 4 are the droplet radii vs height from the steady slow updraught run (dotted lines), which demonstrates that the Ostwald ripening effect (large drop growing at the expense of the smaller) is taking place irrespective of the fluctuations in vertical ascent rate, a finding demonstrated clearly by Celik and Marwitz (1999). The lower panel in Fig. 4 shows the supersaturation against height for the steady updraught run.

Figure 5 shows the equilibrium supersaturation- droplet size curves for the two dry radii mentioned above. Note that in the shaded region the unactivated droplet will grow and the activated one will evaporate. The history of the supersaturation within a parcel therefore is critical in determining whether $s < s_{eq}$ when $r > r_{crit}$ for a particular aerosol category (r_{crit} is the critical radius, i.e. the wet radius at which s_{eq} is a maximum for a particular dry aerosol). The supersaturation in which a particular droplet finds itself is effectively decoupled from the activation of the droplet because of the presence of a spectrum of droplet sizes. Hence, it is possible for the supersaturation (which is controlled largely by the aerosol classes for which the mass growth is largest) to enter the shaded region of Figure 5 and

therefore it is possible for a particular droplet to deactivate once it has been activated.

In all rising parcels with physically realistic updraught speeds and aerosol size distributions, it can be shown that the rate of decrease of supersaturation after the initial sharp peak (e.g. higher than 50 metres above cloud base in Fig. 4(bottom)) is slow, taking several thousand seconds to fall from 1/10 to 1/20 of the peak supersaturation. The simulations of Celik and Marwitz (1999) show a similarly slow decay time for supersaturation. Their parcel was allowed to rise from just below cloud base for 20 minutes. Following the ascent the vertical wind speed was reduced to zero. The peak supersaturation was approximately 0.34% and fell to around 0.03% in approximately 20 minutes. However, it took around three further hours for the supersaturation to fall to 0.015%. This slow decay of supersaturation, which appears to be a feature of all parcel model ascents, allows the Ostwald ripening process to occur over long periods of time.

(d) Droplet size distributions

Figure 6 shows droplet size distributions from the trajectory ensemble model at three different times (60, 180 and 300 minutes) after the start of the simulations. Each size distribution is averaged over the top 200 metres of the cloud layer ($600 < z < 800$ m). Simulations generated using trajectory set A (left panels) are clearly less dispersive than those generated using the weak circulation set B (right panels). The difference in dispersion between the weak and the strong circulations is more marked in the clean aerosol case (both with and without GCCN). The giant CCN has little effect at all upon the droplet size distributions apart from at radii larger than $20 \mu\text{m}$. There is clearly very little evolution of any of the size distributions from simulations using trajectory set A. Significantly more evolution is seen in the trajectory set B simulations which results from the longer in-cloud residence time for parcels in this set.

Because the size distributions presented are averaged over 200 metres of height, it is useful to know how much width in the size distribution is caused by averaging over this range. Because there is little variation of the droplet concentration with height, this source of dispersion arises almost entirely from variations in liquid water content among the contributing parcels. For example, a parcel at $z=600$ m, will have a liquid water content equal to around half that at $z=800$ m. In this case the dispersion caused

by variations in liquid water content within the 200 metre thick averaging layer is approximately 0.06. This is considerably smaller than the dispersion caused by physical processes (rather than averaging) in all cases.

It is found that the concentration N_d of droplets with radii larger than $1 \mu\text{m}$ is always close to the concentration of activated particles. There is little evidence for ripening of the set A droplet size distributions with time after approximately 50 minutes into the simulations, but with set B simulations there is a fall in droplet concentration, a rise in $r > 20\mu\text{m}$ particles and a rise in the number of unactivated aerosol over the course of 300 minutes. This ripening effect is present in both the clean and the polluted simulations, with and without giant CCN. The presence or otherwise of giant CCN makes little difference to the droplet number concentration, but a considerable difference to the concentration of droplets larger than $20 \mu\text{m}$. The time rate of change in droplet number concentration and number of droplets larger than $20 \mu\text{m}$ is much smaller after 300 minutes (not shown) for set B simulations.

The results demonstrating only time evolution of parameters derived from set B simulations is consistent with the in-cloud residence time probability distributions (Fig. 1). For weak circulations (set B), this pdf appears to equilibrate around 6 hours after the start of the simulations. For strong circulations (set A) the in-cloud residence time pdf equilibrates in less than one hour which explains the lack of time evolution of spectral characteristics.

Figure 7 shows the spectral dispersion and mean volume radii as a function of time. All data are taken from the averaged (ensemble) size distributions ($600 < z < 800 \text{ m}$). The spectral dispersion is defined as the standard deviation in radius divided by the mean radius. Set A simulations show little change with time in either of these parameters, whereas the set B volume radii increase with time as the size distributions broaden and the droplet number concentration falls. The timescales for evolution of the volume radius and the spectral dispersion are similar.

(e) Comparison with single parcel ascent

To investigate the effects of parcel circulation and in-cloud residence time we compare the TEM results with two different approaches. In the first approach a single parcel is initialised below cloud

base and rises into the cloud with a vertical ascent rate equal to the standard deviation of vertical wind which is chosen because it represents a measure of the typical strength of the updraughts in the cloud layer.

Table 3 shows mean droplet number concentration (concentration with radii larger than $1 \mu\text{m}$), mean volume radius r_{vol} and dispersion, calculated from the TEM and the single parcel ascent (SP). In each case the data are taken from the height region ($600 < z < 800 \text{ m}$). The TEM results are taken between times 200 and 300 minutes after the start of the simulations so that any Ostwald ripening will have taken place. In all cases the single parcel model produces size distributions with lower dispersions than the TEM. However, for the strong circulations, the ratio of the TEM dispersion to the SP dispersion ranges from 1.19-1.25 whilst for the weak circulations the ratio ranges from 1.63-2.24. In all set B cases the SP dispersions are close to those in the TEM close to the start of the simulations (see Fig. 7), showing that the TEM and SP models dispersion differences in Table 3 are mainly a result of the time development (i.e. ripening) of the TEM size distributions.

The number concentrations and volume radii do not markedly differ between TEM and SP which suggests that the increased TEM dispersion in the weak circulation cases is largely caused by a broadening both to small and larger sizes. This is clearly demonstrated in Fig. 8 which shows the TEM and SP droplet size distributions from which the data in Table 3 were derived. Note that the size distributions are taken from the four case with no giant CCN. In all size distributions the SP model results in very few droplets smaller than $3 \mu\text{m}$. The time evolution of the TEM size distributions (Fig. 6) demonstrate that broadening to small sizes takes place over long timescales with set B trajectories due to the long in-cloud residence times of some of the parcels. However, in all TEM simulations there are considerably more small droplets ($r < 3 - 4 \mu\text{m}$) than there are in the SP simulations. Clearly then some of the higher numbers of small droplets in the TEM are not the result of Ostwald ripening alone since set A simulations experience hardly any size distribution changes at all after 1 hour. The presence of these droplets is likely to be the result of deactivation and reactivation of droplets as the vertical wind changes from negative to positive.

4 Effect upon autoconversion of cloud droplets

From the model droplet size distributions it is possible to compute estimates of the autoconversion of cloud liquid water to drizzle liquid water. Here we use the method of Austin et al. (1995b) to calculate the rate of mass transfer of drops across the $r = 20\mu\text{m}$ boundary. The droplet size distribution between $1 < r < 20 \mu\text{m}$ is obtained from the trajectory ensemble model parcels, and binned onto 60 bins, logarithmically spaced in r . For this example we use the mean size distributions ($600 < z < 800 \text{ m}$) derived as a function of time, although it would be possible to use any height interval one wished. We solve the SCE using the computationally efficient code of Bott (1998), which can be carried out with minimal numerical diffusion using timesteps equal to 10 s. As in Austin et al. (1995b) we define the autoconversion A as the mass transfer rate across the $r = 20\mu\text{m}$ boundary over 10 minutes. This is appropriate because the mass transfer rate is close to constant over the 10 minute period. Collection efficiencies are taken from Hall (1980).

Figure 9 shows the autoconversion calculated from the model size distributions for the clean cases (with and without giant CCN). Simulations with trajectory set A and B initially start with similar autoconversion rates but due to ripening effects in set B, the autoconversion increases rapidly. After 300 minutes in the no GCCN case (Fig. 9(left)) the set B autoconversion rate is over two orders of magnitude larger than for the set A distributions. The effect is less pronounced, but still present, when giant CCN are included. It is interesting that the presence of giant CCN has a huge effect upon the autoconversion rate in general. However, the weak circulations can lead to autoconversion rates almost as large as those in the giant CCN case simply by spectral broadening caused by the ripening process. This suggests that the effects of both giant CCN and spectral ripening (in boundary layer clouds with weak circulations) are integral to the initial production of drizzle in stratiform boundary layer clouds and as such will need to be addressed when deriving parameterizations for use in large scale models.

5 Discussion

In this study we have used an ensemble of parcels moving within a well-mixed cloud-topped boundary layer in an attempt to assess the potential importance of size distribution temporal Ostwald ripening.

Ripening has been shown to broaden the droplet size distribution within a single closed parcel (Celik and Marwitz 1999). This occurs due to a thermodynamic instability which means that large drops tend to grow at the expense of smaller ones leading to a broadening of the droplet size distribution over time *without* the need for supersaturation fluctuations. In turbulent boundary layer clouds the supersaturation does fluctuate. We have demonstrated that the ripening effect occurs only in clouds where the parcel in-cloud lifetimes are sufficiently large for the Ostwald ripening process to occur. A ripening timescale within parcels remaining stationary within a cloud after an initial rise into cloud is a function of the nature of the dynamics and the aerosol physical and chemical properties. It is difficult to define the ripening timescale formally but the process is ultimately controlled by the rate of decay of supersaturation within the parcel. This process tends to occur over timescales of several hours, and results in broader (more dispersive) size distributions with lower droplet concentrations.

The trajectory ensemble has been used to examine the statistics of in-cloud residence time for two sets of trajectories: the first set is typical of fairly vigorous thermals which are typical of convectively driven stratocumulus clouds (e.g. see Nicholls and Leighton 1986, Flight number 526, for an example of this type of cloud dynamical structure). The second set is more characteristic of weaker stratus clouds formed through cooling of an airmass from below or in relatively high wind speed conditions (e.g. see Brost et al. 1982a,b, especially 17 June 1976 flight). The distributions of in-cloud residence time for a 400 m thick cloud shows that there are few parcels in the strong case that are in cloud for more than 50-100 minutes. However, for the weak case a significant proportion of the parcels remain in cloud for over an hour, and some remain in cloud for considerably longer. It is also noted therefore that parcel model ensembles in which some parameters depend strongly upon in-cloud residence time could require several hours of integration before equilibrium is reached. This could be particularly important in studies of both aqueous-phase and gas-droplet chemistry and cloud processing of aerosols, and the interaction of droplets with radiation.

We found, for the cases with long in-cloud residence times, the the size distribution broadened to both small and large sizes for several hours after the start of the simulations. The droplet concentration ($r > 1\mu\text{m}$) falls with time and the number of unactivated particles rises as droplets are de-activated due to the Ostwald ripening process. The number of droplets with radii larger than $20\mu\text{m}$ increases, in both

the clean and polluted cases. The rise is less marked when giant CCN are included because the GCCN provide a source of large droplets in addition to those caused by the ripening process. Autoconversion rates were found to increase in all the weak circulation cases. In contrast, negligible time evolution of parameters is seen in any of the strong circulation cases. These results show that to accurately model the droplet size distribution in weakly turbulent boundary layer clouds, it is necessary to account for the possible slow microphysical temporal evolution. In addition, the response of cloud layers to changes in their turbulent structure can in some cases be particularly slow, with clouds possessing long microphysical memories of previous dynamical structure.

Upon examining the microphysical evolution during ascent, it is apparent that the only requirement for the ripening process to occur is time. Thus, a parcel with a slow ascent will take longer to reach a particular level and will therefore have had more ripening time. Fluctuations in ascent rate have little effect *per se*, but they are likely to cause a parcel to remain in cloud for longer.

The simulations presented in this study did not include the effects of entrainment, radiative growth or parcel-parcel mixing. Stevens et al. (1996) find that entrainment across cloud top is a large source for size distribution dispersion. However, it is not known how entrainment will affect the results presented here, in terms of the ripening of size distributions with time. It will be an interesting study to carry out using TEM with LES-derived trajectories which can include the effects of entrainment mixing. Radiative growth may well increase the temporal evolution effects because large droplets will grow in parcels with long cloud-top residence times. Parcel-parcel mixing is impossible to simulate using the TEM framework presented here. As Korolev (1995) points out, a parcel is likely to mix with the cloud environment within a matter of minutes. The TEM presented here requires the concept of a parcel as a distinct entity existing for several hours without any explicit external interactions. This concept is unlikely to be true in reality. Nevertheless, this is not likely to affect significantly the residence time of droplets in cloud, although it is likely that the supersaturation history of parcels may be affected. Whether parcel-parcel mixing leads to more or less ripening of the droplet size distribution is a subject for future research. It might be possible to simulate effects of parcel-parcel mixing using a two-dimensional size distribution (Bott 2000) which allows binning of the droplet size distribution without losing information about the CCN within the droplets.

6 Acknowledgements

I am grateful to colleagues in the Met Office, particularly at the Met Research Flight, for discussions which aided the research presented in this paper. Sarah Irons was supported by a Natural Environment Research Council PhD scholarship.

7 Appendix: Simulation of turbulent parcel motion

Calculation of the transient matrix elements for very small vertical grid spacings is computationally prohibitive (the number of operations scales approximately with the square of the number of levels used because (a) there is a cubic relationship between the number of operations required for square matrix multiplication and the number of levels; (b) the number of multiplications required decreases approximately linearly with the number of levels). We found that computation of the transient matrix was readily possible for grid spacings of 5-10 m (with 100 levels). The standard deviation in vertical wind speed in stratus/stratocumulus is usually within the range $0.2 < \sigma_w < 0.8 \text{ m s}^{-1}$. In order to generate realistic physical behaviour of the trajectory dynamics, a long enough transient matrix timestep δt_{trans} should be chosen so that there is a reasonable possibility that parcels can jump at least one level per timestep. In this study we chose $\delta t_{trans}=240 \text{ s}$, so that even trajectories for the lowest σ_w would satisfy this condition.

It is clear that real atmospheric trajectories in turbulent boundary layers will be subject to considerable fluctuations in ascent rate on timescales shorter than δt_{trans} . We added fluctuations on all timescales between δt_{trans} and δt_{micro} using a bounded additive cascade model (Marshak et al. 1994; Cahalan et al. 1994). This model leads to a power spectrum which exhibits Kolmogorov scaling (i.e. the power spectral density of the vertical wind along the Lagrangian trajectory is proportional to $(\text{frequency})^{-5/3}$). To achieve this the vertical wind time series along a trajectory was derived from the height-time series. This series was converted to a time series with spacing δt_{micro} using a cubic spline interpolator. Short sections of turbulent time series (each with total time δt_{trans} and timestep δt_{micro} , i.e. $240/0.1=2400$ data points) with zero mean were generated using the cascade model and added back-to-back to the spline-interpolated trajectory series. The total variance contained in timescales

shorter than δt_{trans} was chosen to match the power observed in the trajectory-derived vertical wind at δt_{trans} . Finally, the $(1/\delta t_{micro}$ Hz) height-time series for the trajectory was calculated by integration of the vertical wind time series.

Time series for an example trajectory is shown in Fig. 11. The upper panel shows the trajectory height as a function of time for the case where no small-scale turbulence is added (dashed) and when turbulence is added (solid). The bottom line shows the vertical parcel speed as a function of time for the case of no turbulence (grey) and with turbulence (solid black).

To assess the physical realism of the resulting trajectories we calculated pdfs, autocorrelation functions and power spectra of the vertical wind. Figure 10 and shows pdfs of w plotted using linear (a) and logarithmic (b) ordinates (five example trajectories are shown). All trajectories were calculated with $\tau_w = 250$ s, and $\sigma_w = 0.2$ m s⁻¹. In each case the pdf of the vertical wind speed demonstrates near-Gaussian behaviour (shown by the thick solid line), as expected. Normalised Lagrangian autocorrelation functions $R/R(0)$ and Lagrangian power spectra are shown in Figures 10(c) and (d) respectively. The solid line in Fig. 10(c) is the autoconversion function:

$$R(r) = \sigma_w^2 \exp(-|r|/\lambda_w) \quad (11)$$

which corresponds to the idealised power spectrum used to derive the elements of the transilient matrix (Austin et al. 1995b), i.e.

$$S(k) = \frac{2}{\pi} \left(\frac{\sigma_w^3 \tau_w}{1 + \sigma_w^2 \tau_w^2 k^2} \right) \quad (12)$$

where $\lambda_w (= \sigma_w \tau_w)$ is the Eulerian integral length scale, r is the lag distance, and k is the wavenumber. Autocorrelation functions and power spectra calculated from the simulated trajectories should match those given by Eqns. 11 and 12 respectively if the Eulerian and Lagrangian integral scales are approximately equal. If we make this assumption, then it can be seen from Fig. 10(c),(d) that the agreement between simulated and idealised spectra is reasonably good. Lenschow and Stankov (1984) demonstrate that the idealised autocorrelation functions almost identical in form (at wavenumbers around and smaller than the spectral peak) to those above match quite well with observations of power

spectra in convective boundary layers. This gives us some confidence that the simulated trajectories in this study are representing realistic boundary layer motions.

The spline interpolation was found to lead to very little power at timescales larger than δt_{trans} . Without the addition of the small scale turbulent motions (i.e. with only the effect of the spline interpolation to provide power), the vertical wind power spectra contain at least two orders of magnitude less power at frequencies greater than approximately $1/\delta t_{trans}$. This is the case even when only very low levels of small scale turbulence was added to the transilient trajectories.

References

- Austin, P., Siems, S., and Wang, Y. (1995a) Constraints on droplet growth in radiatively cooled stratocumulus clouds *J. Geophys. Res.*, **100**, 14231–14242.
- Austin, P., Wang, Y., Pincus, R., and Kujala, V. (1995b) Precipitation in stratocumulus clouds: observational and modelling results. *J. Atmos. Sci.*, **52**, 2329–2352.
- Bartlett, J. T., and Jonas, P. R. (1972) On the dispersion of the sizes of droplets growing by condensation in turbulent clouds *Quart. J. Roy. Meteorol. Soc.*, **98**, 150–164.
- Baumgardner, D., Strapp, W. and Dye, J. E. (1985) Evaluation of the forward scattering spectrometer probe. Part II: Corrections for coincidence and dead-time losses. *J. Atmos. Oceanic Technol.*, **2**, 626–632.
- Beard, K. V. and Ochs III, H. T. (1993) Warm-rain initiation: An overview of microphysical mechanisms. *J. Appl. Meteorol.*, **32**, 608–625.
- Bott, A. (1998) A flux method for the numerical solution of the stochastic collection equation. *J. Atmos. Sci.*, **55**, 2284–2293.
- Bott, A. (2000) A flux method for the numerical solution of the stochastic collection equation: Extension to two-dimensional particle distributions. *J. Atmos. Sci.*, **57**, 284–295.
- Brenguier, J-L., Bourrienne, T., De Araujo Coelho, A., Isbert, J., Paytavi, R., Trevarin, D. and Weschler, P. (1998) Improvements of droplet size distribution measurements with the Fast-FSSP (Forward Scattering Spectrometer Probe). *J. Atmos. Oceanic Technol.*, **15**, 1077–1090.
- Brenguier, J-L. and Chaumat, L. (2000) Droplet spectral broadening in cumulus clouds. Part I: Broadening in adiabatic cores. submitted to *J. Atmos. Sci.*

Brost, R. A., Lenschow, D. H., and Wyngaard, J. C. (1982a) Marine stratocumulus layers. Part I: Mean conditions *J. Atmos. Sci.*, **39**, 800-817.

Brost, R. A., Wyngaard, J. C., and Lenschow, D. H. (1982b) Marine stratocumulus layers. Part II: Turbulence budgets *J. Atmos. Sci.*, **39**, 818-836.

Cahalan R. F., Ridgway, W., Wiscombe, W. J., Bell, T. L. & Snider, J. B. (1994) The albedo of fractal stratocumulus clouds. *J. Atmos. Sci.*, **51**, 2434-2455.

Celik F. and Marwitz, J. D. (1999) Droplet spectral broadening by ripening process. Part I: Roles of curvature and salinity of cloud droplets. *J. Atmos. Sci.*, **56**, 3091-3105.

Dye, J. E. and Baumgardner D. (1984) Evaluation of the Forward Scattering Spectrometer Probe. Part I: Electronic and Optical Studies. *J. Atmos. Oceanic Technol.*, **1**, 329-344.

Fitzgerald, J. W. (1972) A study of the initial phase of cloud droplet growth by condensation: comparison between theory and observation. *PhD dissertation*, pages Dept. of Geophys. Sci., University of Chicago.

Fukuta, N. and Walter, L. A. (1970) Kinetics of hydrometeor growth from a vapor-spherical model. *J. Atmos. Sci.*, **27**, 1160-1172.

Hall, W. D. (1980) A detailed microphysical model within a two-dimensional dynamic framework: Model description and preliminary results. *J. Atmos. Sci.*, **37**, 2486-2507.

Howell, W. E. (1949) The growth of cloud drops in uniformly cooled air. *J. Meteorol.*, **6**, 134-149.

- Korololev, A. V. (1995) Effect of supersaturation fluctuations on droplet size spectra formation. *J. Atmos. Sci.*, **52**, 3620–3634.
- Lenschow, D. H. and Stankov, B. B. (1984) Length scales in the convective boundary layer. *J. Atmos. Sci.*, **43**, 1198–1209.
- Marshak, A., Davis, A., Cahalan, R. F., Wiscombe, W. J. (1994) Bounded cascade models as non-stationary multifractals. *Phys. Rev.*, **E49**, 55–79.
- Nicholls, S., and Leighton, J. (1986) An observational study of the structure of stratiform cloud sheets: Part I. Structure *Quart. J. Roy. Meteorol. Soc.*, **112**, 431–460.
- Nicholls, S. (1987) A model of drizzle growth in warm, turbulent, stratiform clouds. *Quart. J. Roy. Meteorol. Soc.*, **113**, 1141–1170.
- O’Dowd, C. D., Smith, M. H., Consterdine, I. E., and Lowe, J. A. (1997) Marine aerosol, sea-salt, and the marine sulphur cycle: A short review. *Atmos. Environ.*, **31**, 73–80.
- Pruppacher, H. R. and Klett, J. D. (1997) *Microphysics of clouds and precipitation* Second edition, Kluwer Academic Publishers, 994pp.
- Srivastava, R. C. (1991) Growth of cloud drops by condensation: effect of surface tension on the dispersion of drop sizes. *J. Atmos. Sci.*, **48**, 1596–1605.
- Stephens, G. L. (1978) Radiation profiles in extended water clouds. I: Theory. *J. Atmos. Sci.*, **35**, 2111–2122.
- Stevens, B., Feingold, G., Cotton, W. R., and Walko, R. L. (1996) Elements of the microphysical structure of numerically simulated nonprecipitating stratocumulus. *J. Atmos. Sci.*, **53**, 980–1006.

Stull, R. B. (1984)

Transient turbulence theory. Part I: The concept of eddy mixing across finite differences. *J. Atmos. Sci.*, **41**, 3351–3367.

Tang, I. N. and Munkelwitz, H. R. (1994) Water activities, densities, and refractive indices of aqueous sulphates and sodium nitrate droplets of atmospheric importance. *J. Geophys. Res.*, **99**, 18801-18808.

Wendisch, M., Keil, A. and Korolev, A. V. (1996) FSSP characterization with monodisperse water droplets *J. Atmos. Oceanic Technol.*, **13**, 1152–1165.

Table 1: Details of trajectory ensembles used in this study

Ensemble	N_{traj}	σ_w [m s ⁻¹]	τ_w [s]	z_b [m]	z_i [m]	$\bar{\tau}_{in,\infty}$ [min]	t_0 [min]
A	200	0.6	330	400	800	10	14
B	200	0.2	250	400	800	95	160

Table 2: Details of simulations used in this study

Simulation	Trajectory set	Small CCN	Giant CCN
	[A (strong) or B (weak)?]	[Clean or Polluted?]	[Yes/No?]
SCN	A	Clean	No
SCG	A	Clean	Yes
SPN	A	Polluted	No
SPG	A	Polluted	Yes
WCN	B	Clean	No
WCG	B	Clean	Yes
WPN	B	Polluted	No
WPG	B	Polluted	Yes

Table 3: Comparison between parcel model approaches. Data for TEM and SM simulations are averaged over the height range $600 < z < 800$ m, for TEM values averages are taken over times 200-300 minutes after start of simulations.

Simulation	N_d		r_{vol}		Dispersion	
	[cm^{-3}]		[μm]			
	TEM	SP	TEM	SP	TEM	SP
SCN	191	163	8.80	9.28	0.094	0.075
SCG	190	170	8.84	9.14	0.124	0.099
SPN	747	683	5.65	5.76	0.188	0.155
SPG	737	684	5.67	5.76	0.204	0.172
WCN	138	113	10.07	10.48	0.173	0.106
WCG	138	126	9.95	10.12	0.224	0.127
WPN	319	339	7.57	7.27	0.365	0.163
WPG	315	340	7.53	7.27	0.381	0.210

Figure captions

Figure 1. The mean time that a sampled parcel ($400 < z < 800$ m) has been in cloud, plotted as a function of time after the start of the simulation (top left panel). The solid line (trajectory set A) is for the strong convective case; the dashed line (set B) is for the case of weaker circulations. The dotted lines are explained in the text. Standard deviation of τ_{in} plotted as a function of the mean value (top right panel). Probability density functions for τ_{in} derived for the set A (lower left panel) and set B (lower right panel) trajectories. Clearly, while there is little evolution of the set A residence time pdf, the set B pdf is evolving over several hours.

Figure 2. Plot of $\bar{\tau}_{in,\infty}$ and t_0 (Eqn. 10) as a function of cloud thickness for trajectory sets A (triangles) and B (circles). The error bars show 95% confidence limits.

Figure 3. Aerosol number (left) and mass (right) distributions used in this study. The polluted and clean modes are both modelled as lognormal distributions with number modal radius of $0.04 \mu\text{m}$, geometrical standard deviation of 2.2, and number concentrations of 1000 cm^{-3} and 200 cm^{-3} respectively. The giant mode has a distribution with lognormal parameters and number concentration given by the spume drop parameterization of O'Dowd and Smith (1993). If a particular simulation includes giant CCN then this mode is simply added to either the clean or polluted mode.

Figure 4. Example of droplet growth in simulations with weak (solid lines) and strong (dashed lines) updraughts. The upper panel shows the height-time series for three example trajectories, one of which (dashed line) ascends more rapidly. The dotted line represents a steady ascent at the same mean ascent rate as the solid line. The central panel shows the size of droplets formed on two dry aerosol sizes ($a = 0.05 \mu\text{m}$, thin lines; $a = 0.6 \mu\text{m}$, thick lines). Large droplets have more time to grow, and small droplets more time to shrink, in the slowly ascending parcels which results in broader size distributions at all heights in the cloud. The fluctuation in ascent rate in the non-steady case is not a prerequisite for ripening to occur. The lower panel shows the supersaturation as a function of height from the steady-ascent run.

Figure 5. Equilibrium supersaturation curves for dry ammonium sulphate particles with radii of $0.05 \mu\text{m}$ (dashed line) and $0.6 \mu\text{m}$ (solid line). The shaded area represents that part of the droplet radius-supersaturation phase space for which an activated $a = 0.05\mu\text{m}$ droplet will evaporate at the expense of an unactivated $a = 0.6\mu\text{m}$ droplet.

Figure 6. Time evolution of the eight droplet size distributions. The size distributions at 60 minutes (solid), 180 minutes (dotted) and 300 minutes (dashed) after the start of the simulations are shown in each case. There is negligible evolution of the size distribution of droplets formed with trajectory set A, but those formed using set B continue to broaden with time towards both smaller and larger sizes. Data are all taken from the top half of the cloud ($600 < z < 800 \text{ m}$).

Figure 7. Time evolution of the radius dispersion $\sigma_{r,ens}$ of the averaged size distribution ($600 < z < 800 \text{ m}$) and the mean volume radius r_{vol} for the four cases with no giant CCN. Polluted cases (thin lines) show generally broader size distributions (larger dispersions) than the clean cases (thick lines). Set B cases are generally broader and show considerable time evolution. The clean cases have larger values of r_{vol} throughout the simulations. The value of r_{vol} increases in the set B simulations reflecting the decrease in activated droplet concentration with time. The inclusion of GCCN made almost no change to the mean volume radius.

Figure 8. Comparison of trajectory ensemble model (TEM, solid lines) and single parcel model (SP, dashed lines) drop size distributions for clean and polluted conditions (no GCCN). In all cases the SP model produces considerably narrower distributions and an absence of the smallest droplets.

Figure 9. Autoconversion rates as a function of time calculated from TEM model distributions for clean simulations, with (left) and without (right) giant CCN. Autoconversions are higher for the weak circulations and increase with time during the 300 minutes shown. In the no GCCN case the increase is greater than two orders of magnitude.

Figure 10. Example of trajectory diagnostics for the weak circulation case (set B). Vertical wind pdfs (upper panels, right using logarithmic ordinate). Five trajectories are shown here. The thick solid line

shows the Gaussian distribution with standard deviation $\sigma_w = 0.2\text{m s}^{-2}$. The lower left panel shows the normalised Lagrangian autocorrelation function of the parcel ascent rate (vertical wind). The thick solid line is explained in the text. The lower right panel shows the vertical wind power spectral density. The thick dashed line exhibits Kolmogorov (“-5/3”) scaling. The thick solid line is described in the text.

Figure 11. Time series of parcel height (top) and ascent rate (bottom) for an example parcel taken from trajectory set B (weak circulation). In the upper panel the solid line includes the effects of small scale turbulence; the dashed line does not. In the lower panel the black line includes the small-scale turbulent fluctuations; the grey line does not.

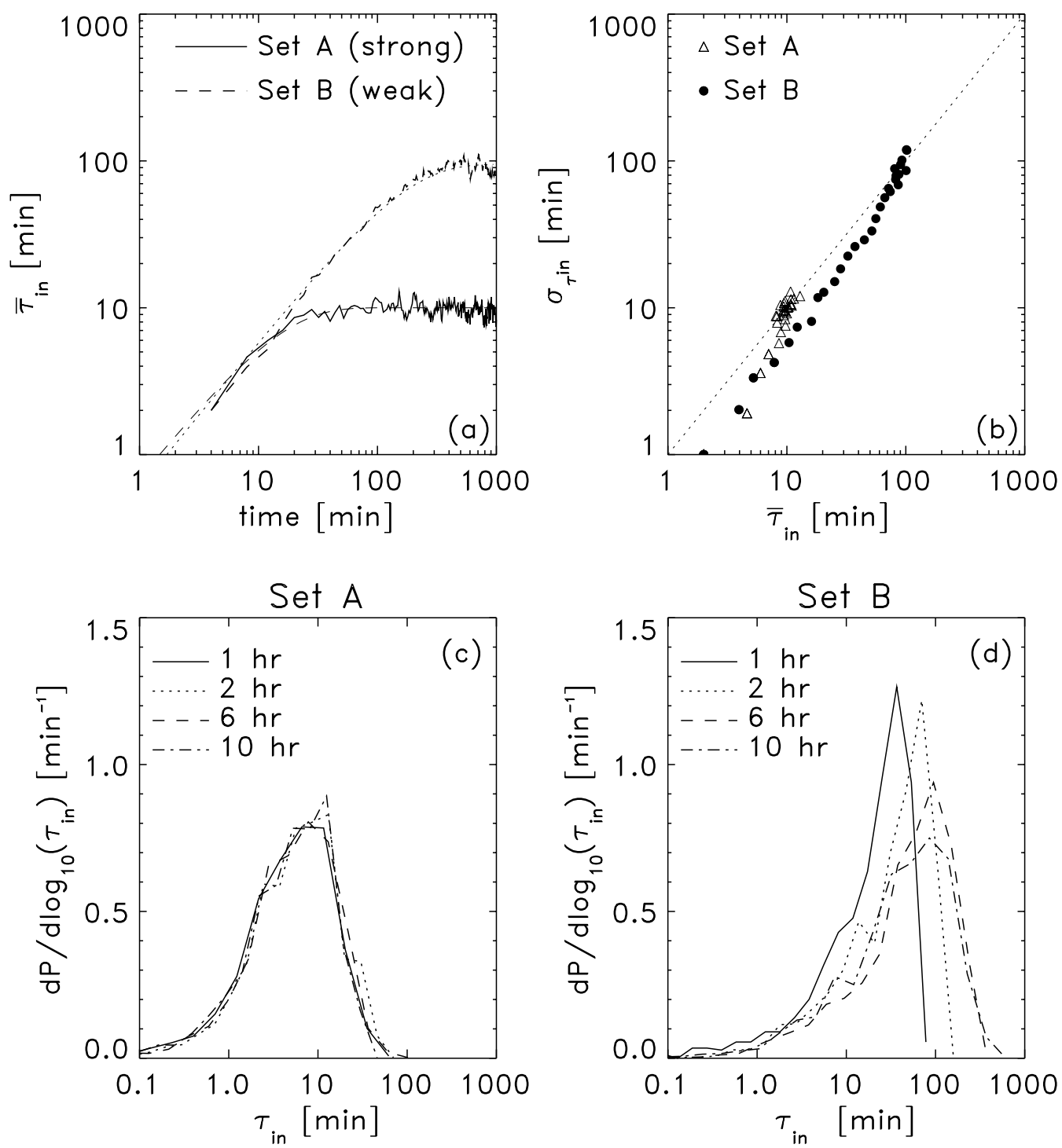


Figure 1:

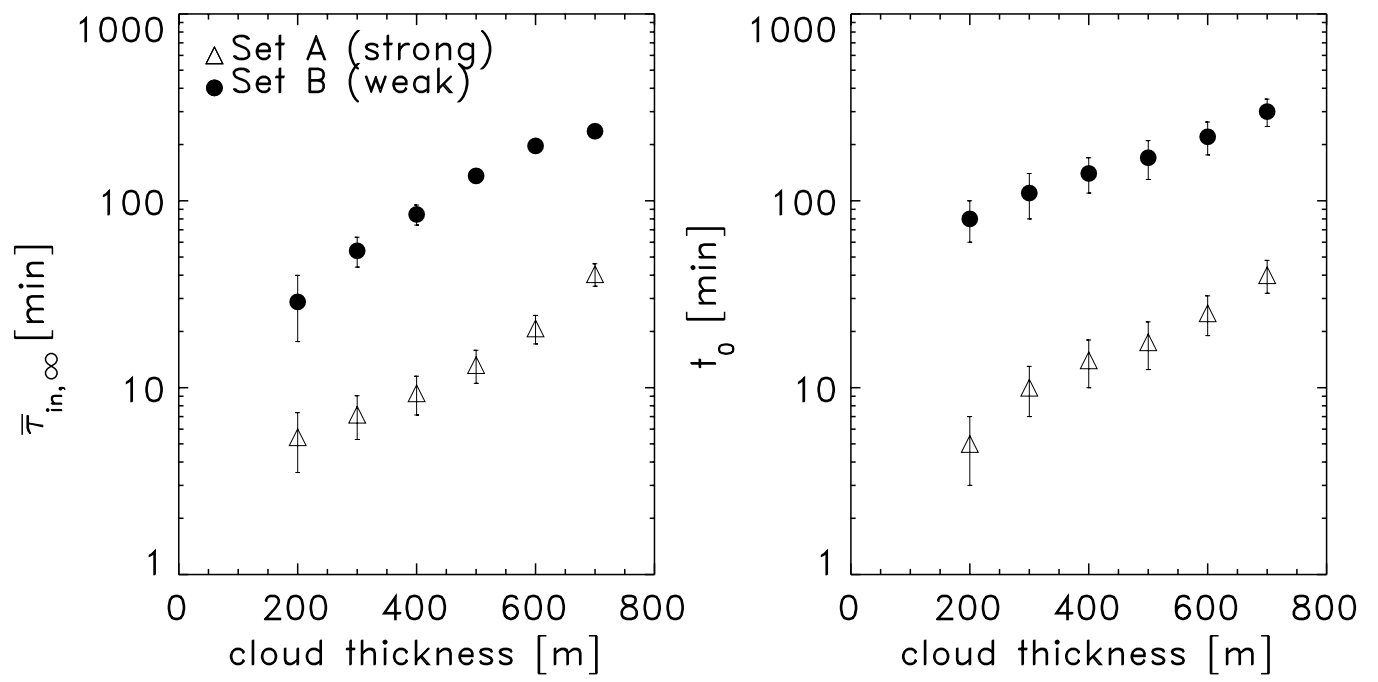


Figure 2:

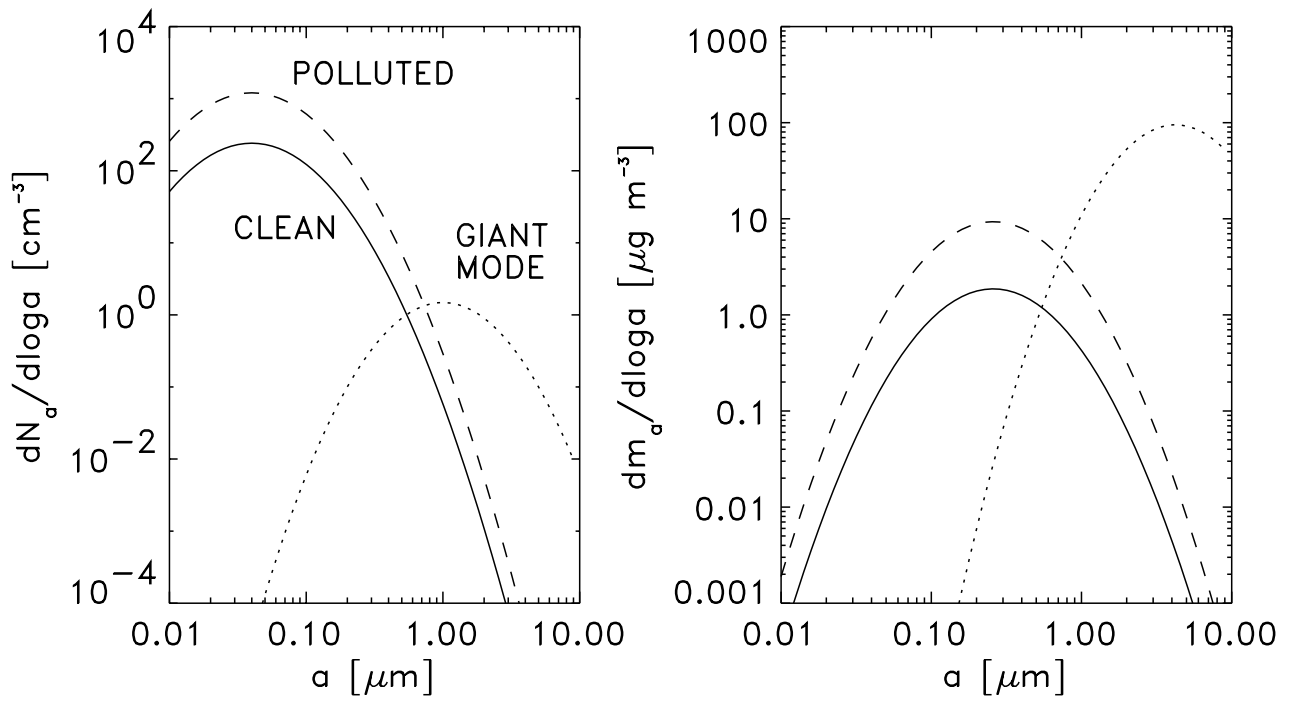


Figure 3:

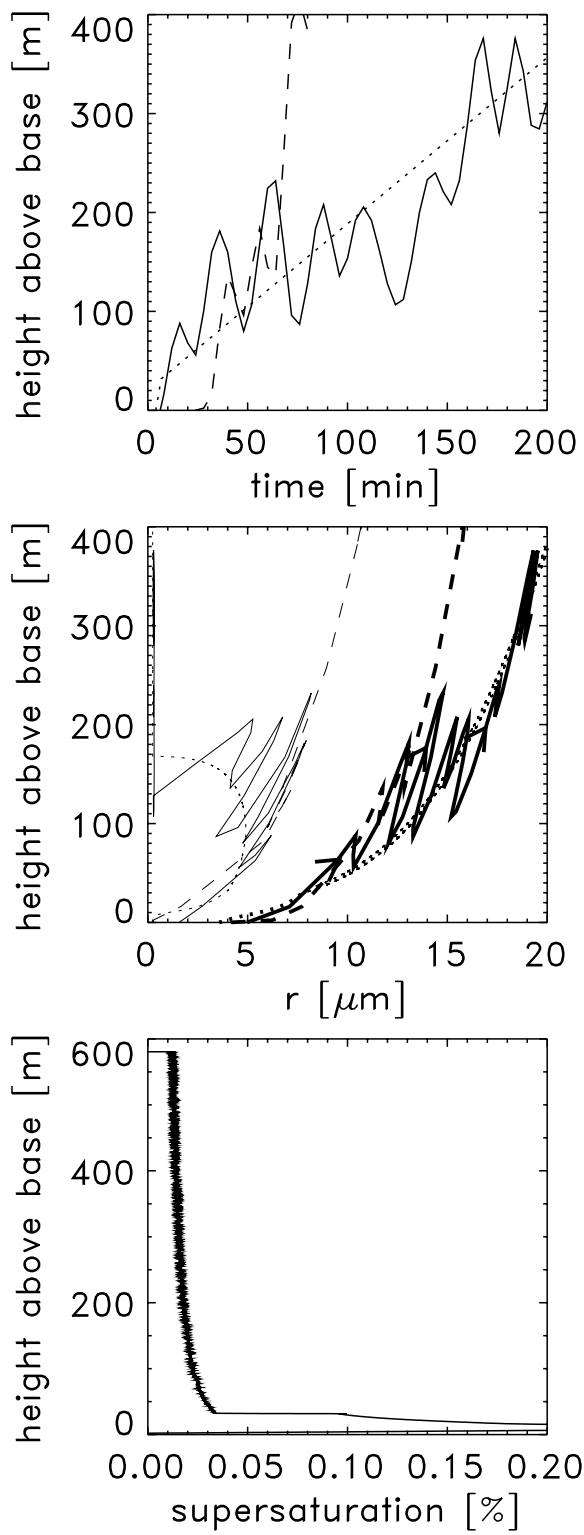


Figure 4:

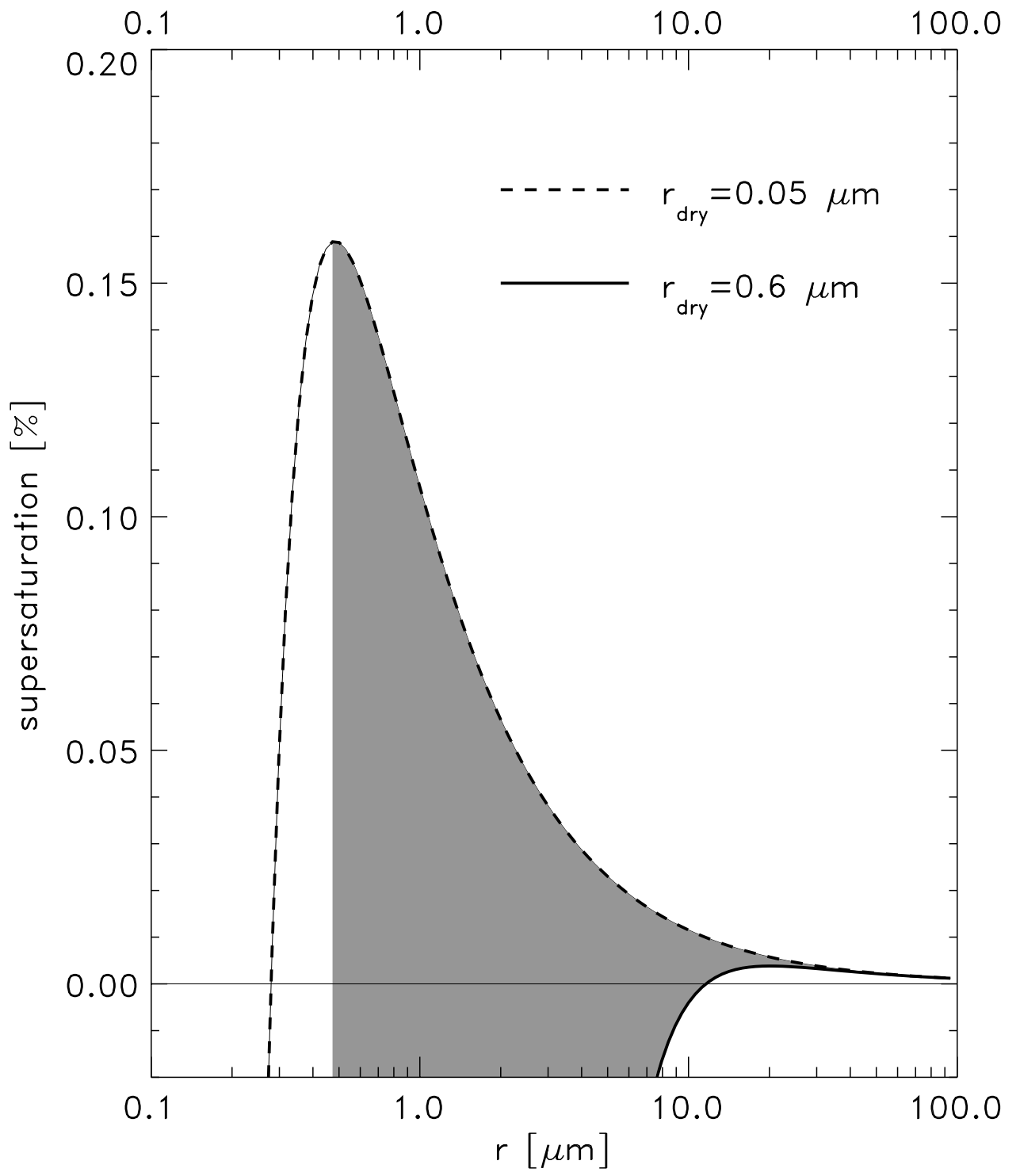


Figure 5:

Without GCCN

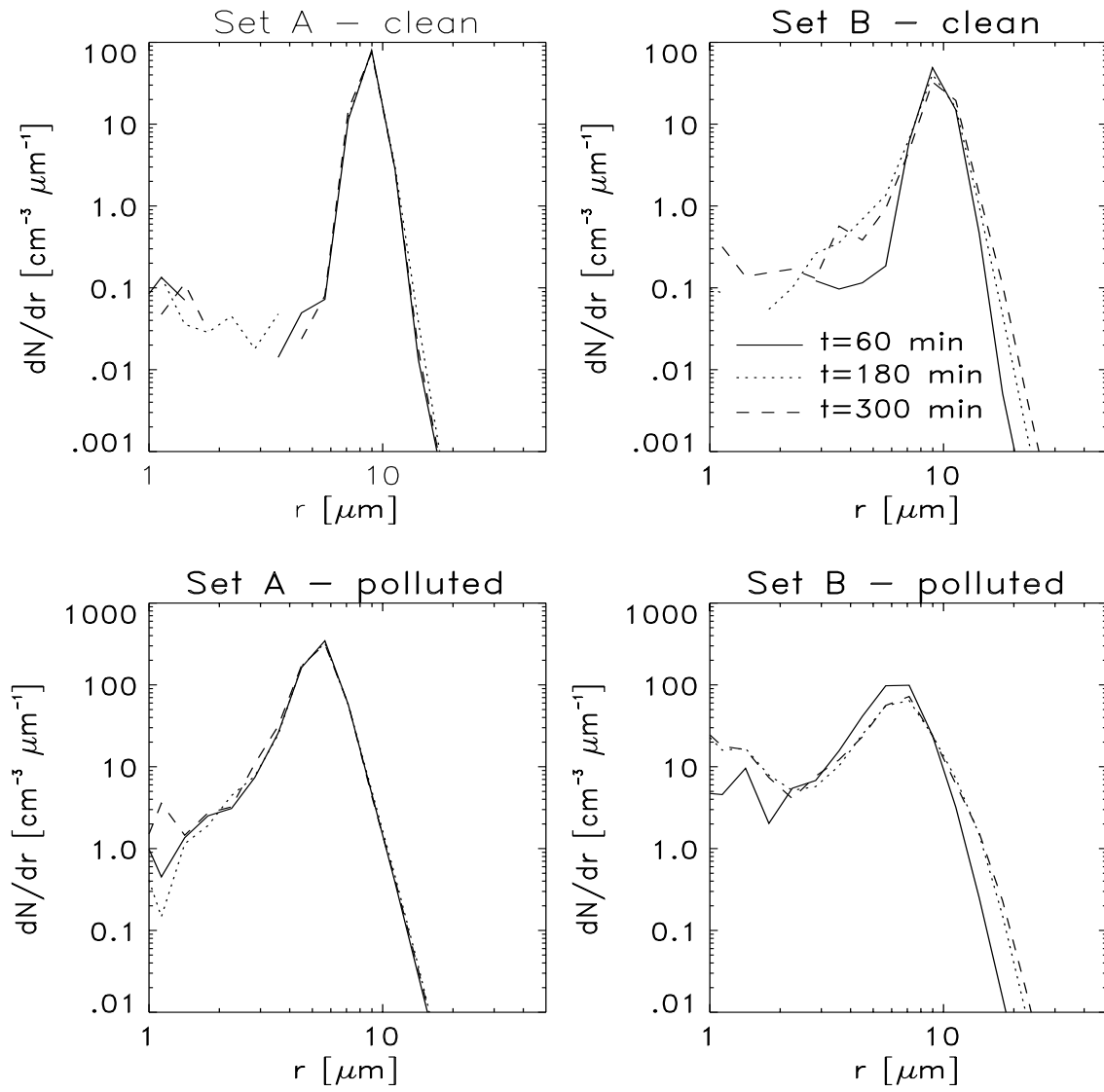
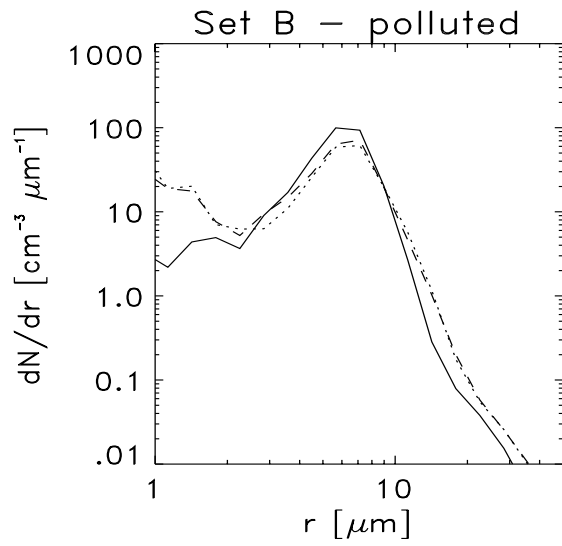
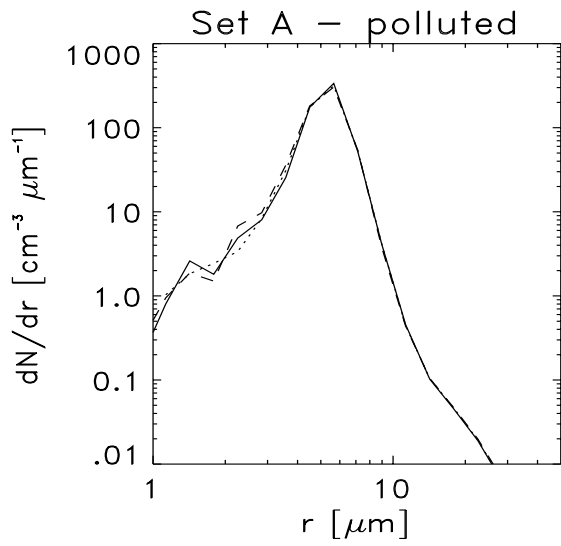
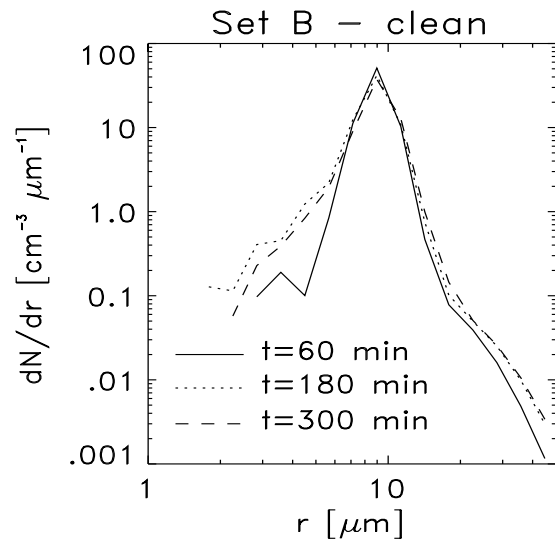
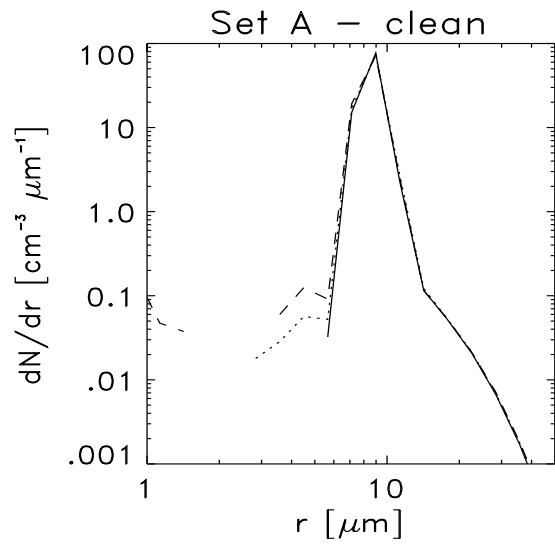


Figure 6:

With GCCN



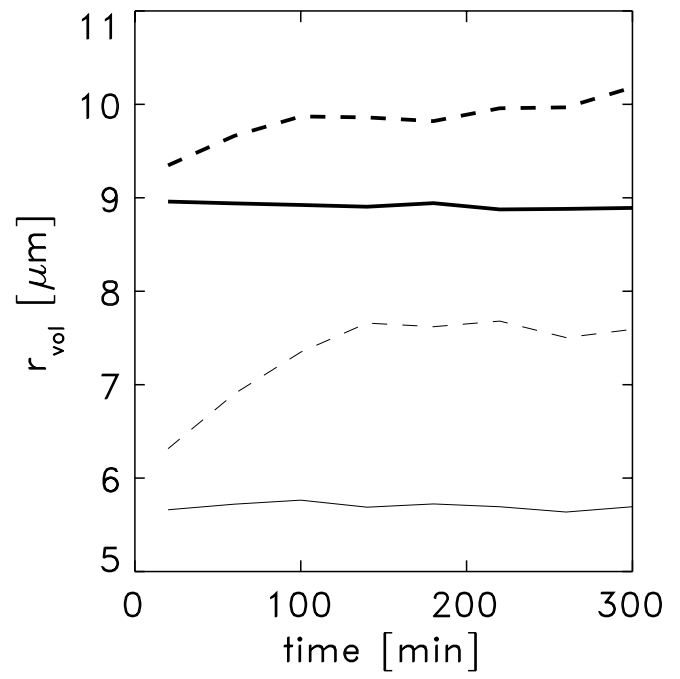
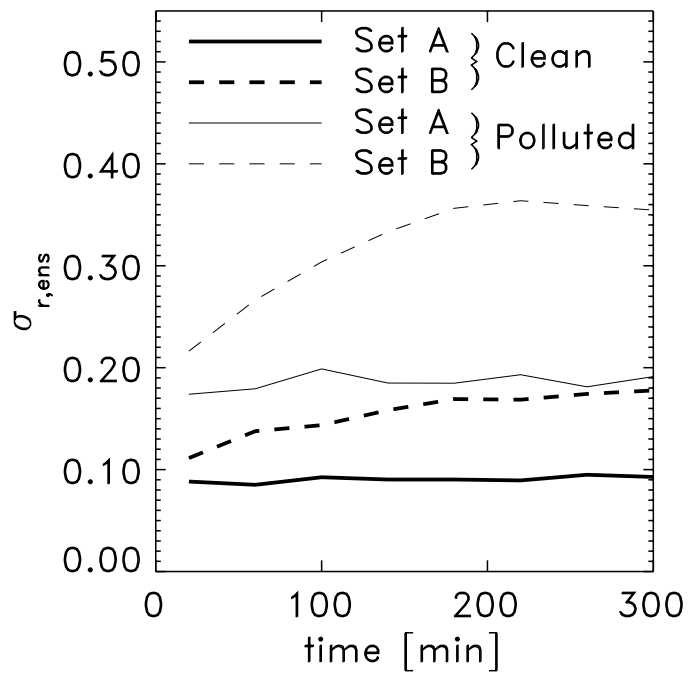


Figure 7:

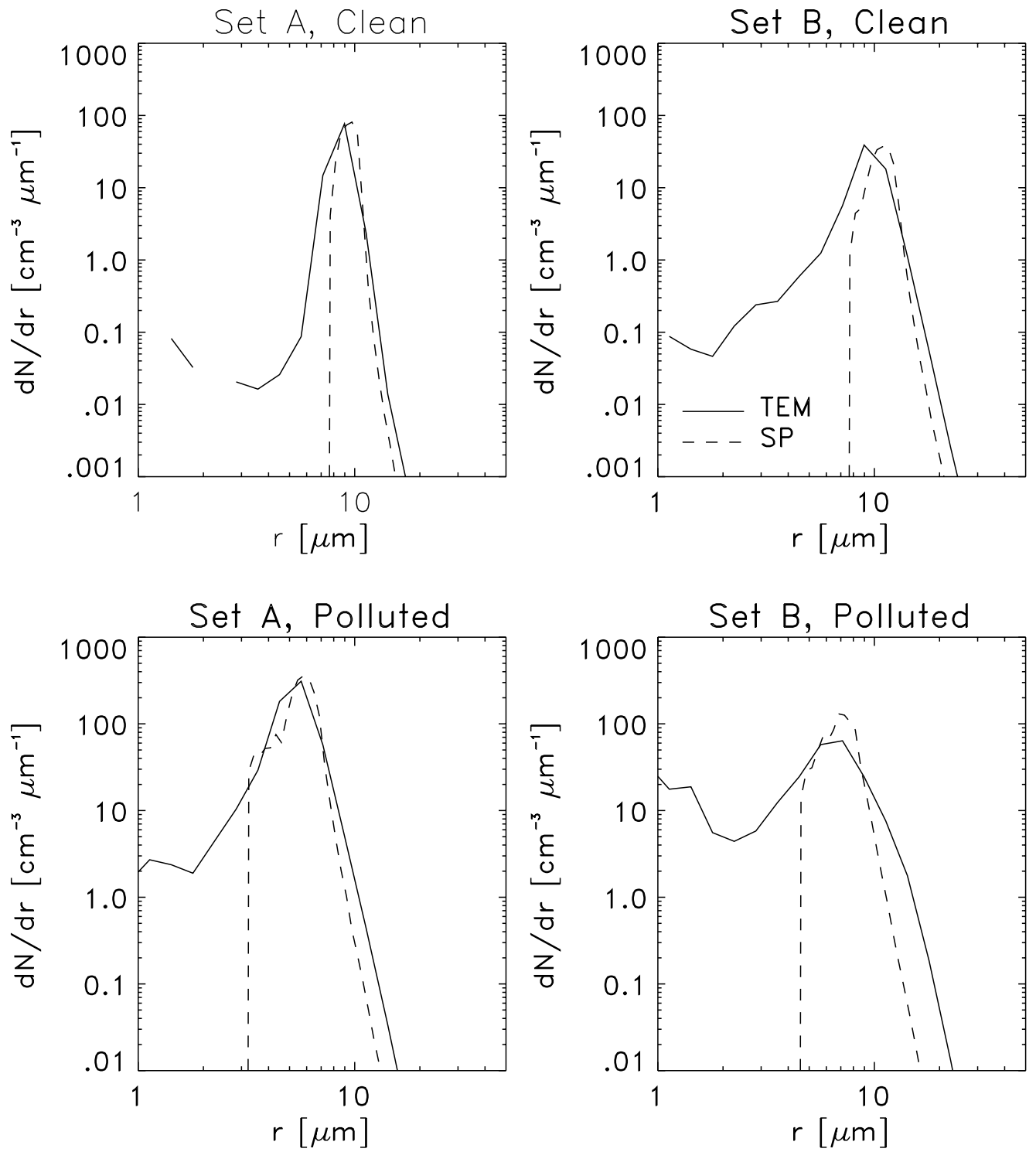


Figure 8:

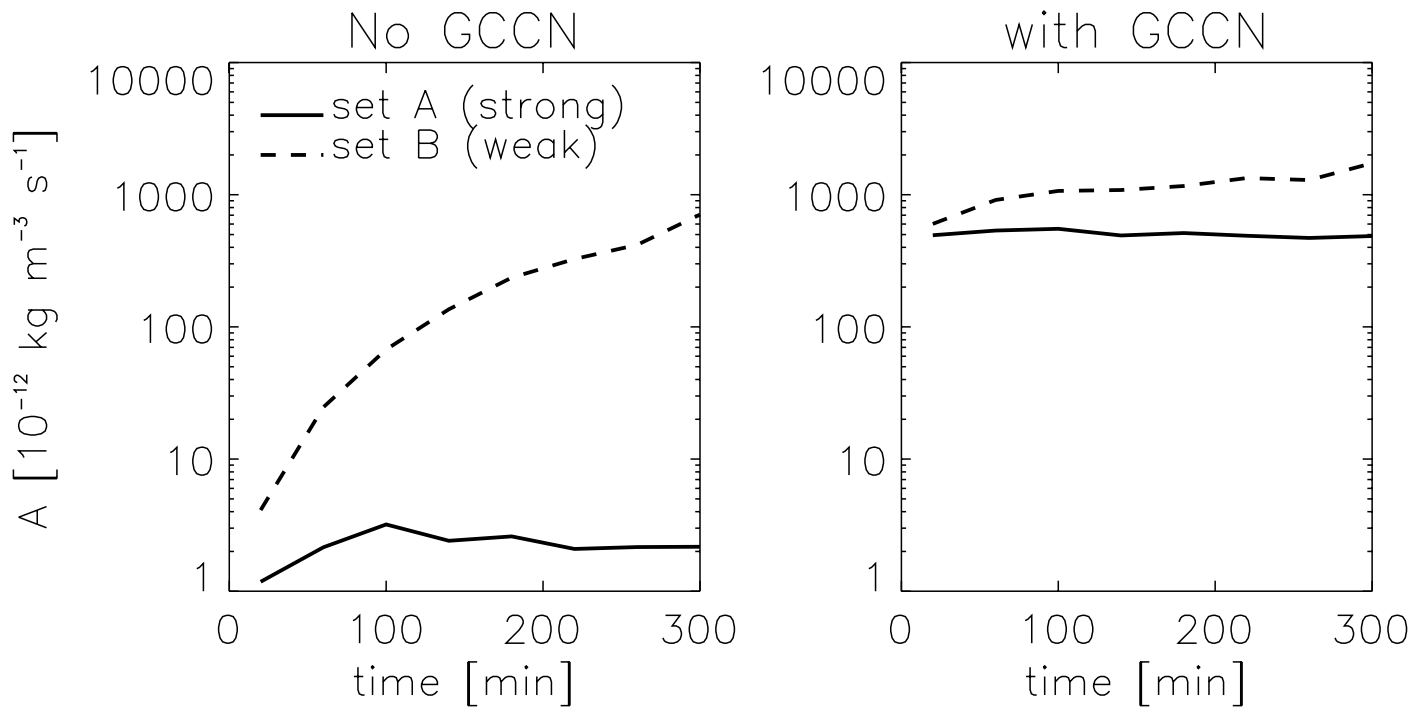


Figure 9:

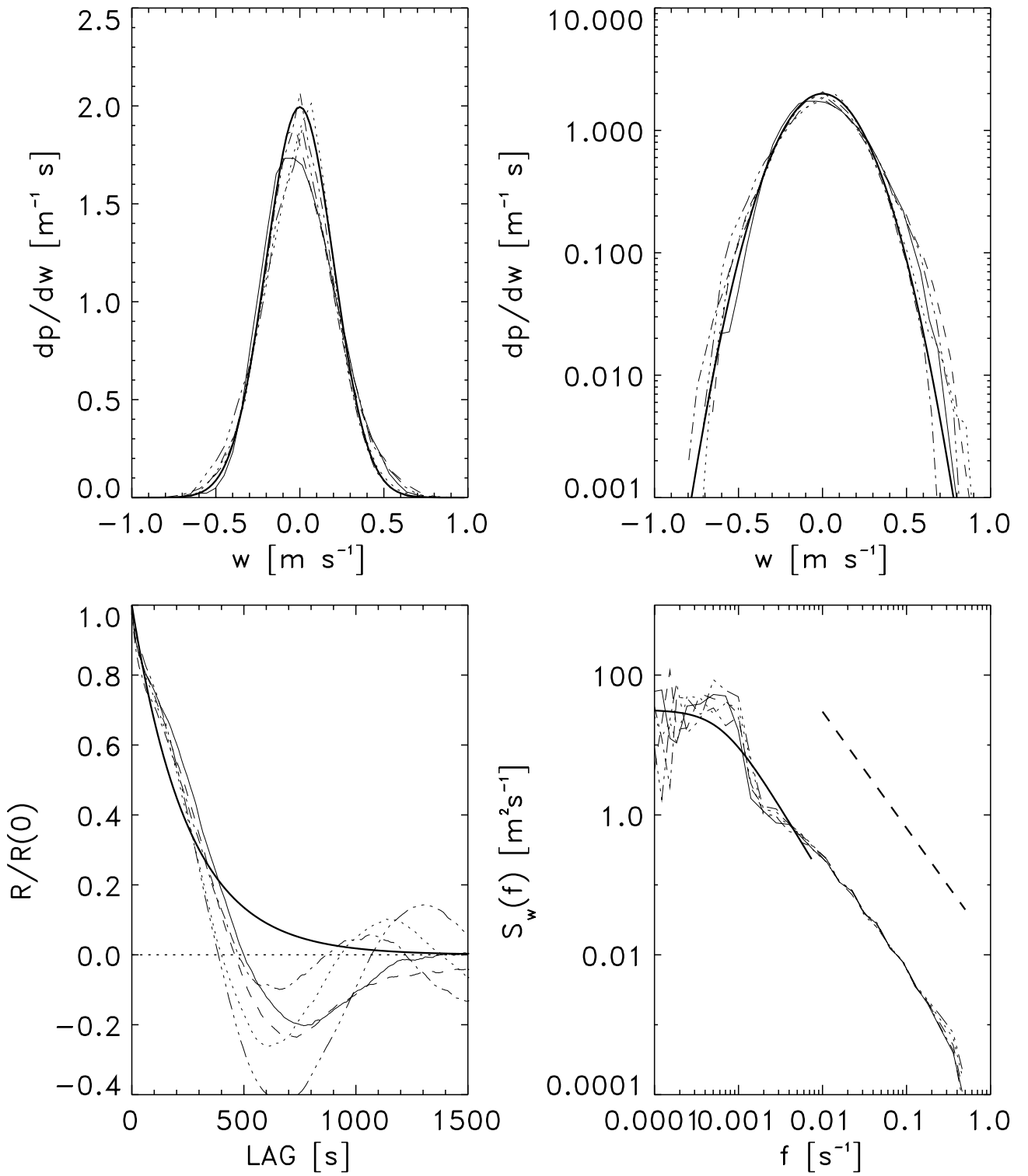


Figure 10:

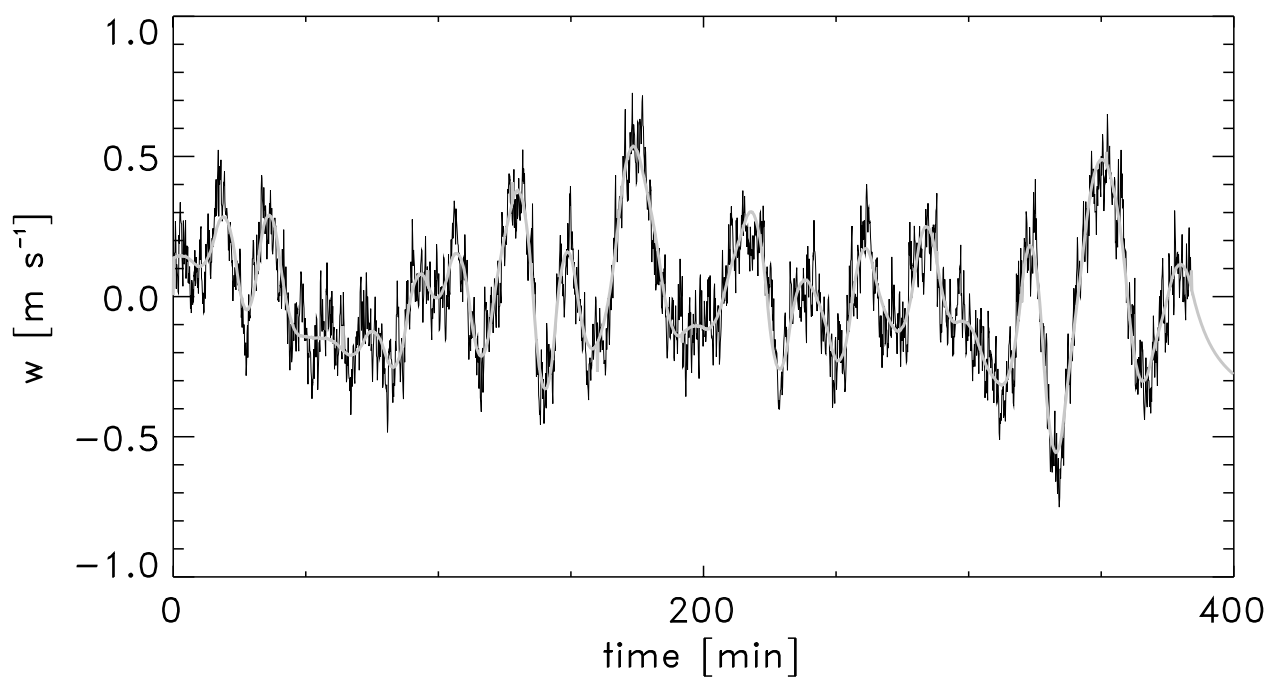
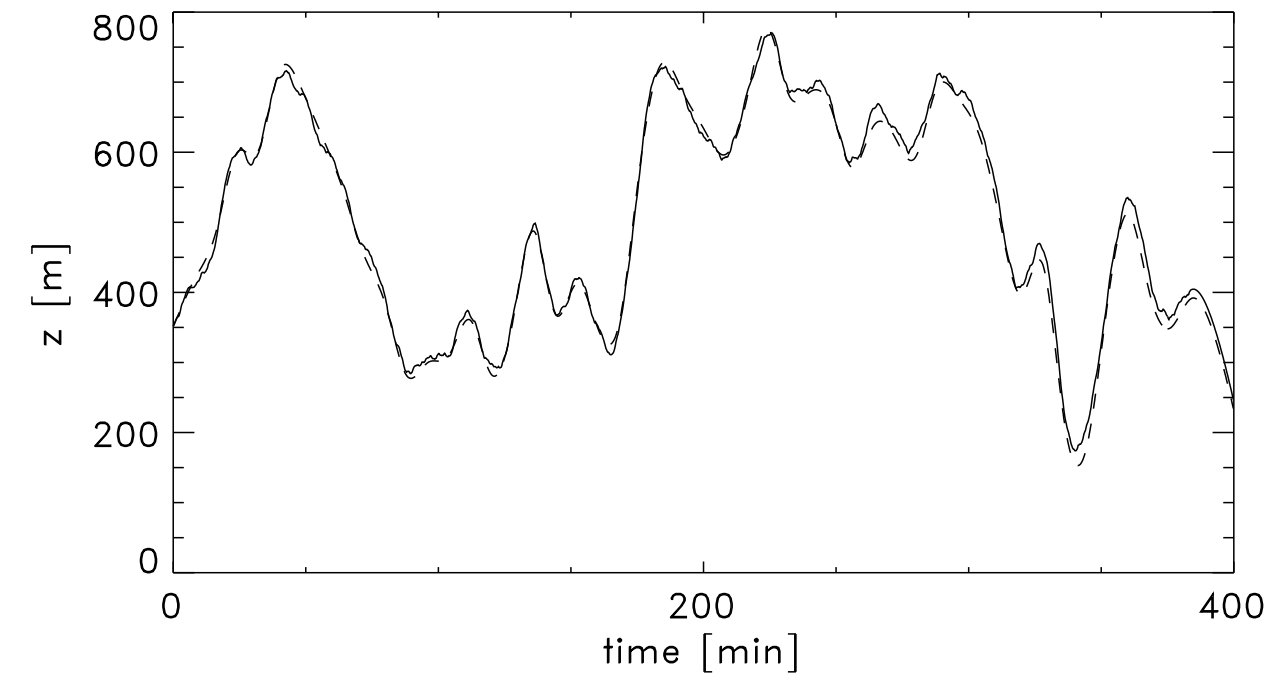


Figure 11: